Integral momentum balance on a growing bubble

S. Siedel, S. Cioulachtjian, A. J. Robinson, and J. Bonjour

Citation: Physics of Fluids (1994-present) **25**, 123301 (2013); doi: 10.1063/1.4844416
View online: http://dx.doi.org/10.1063/1.4844416
View Table of Contents: http://scitation.aip.org/content/aip/journal/pof2/25/12?ver=pdfcov
Published by the AIP Publishing

PHYSICS OF FLUIDS **25**, 123301 (2013)

Integral momentum balance on a growing bubble

S. Siedel,[1,a)] S. Cioulachtjian,[1] A. J. Robinson,[2] and J. Bonjour[1,b)]
[1]*INSA-Lyon, CETHIL, UMR5008, CNRS, F-69621, Villeurbanne, France and Université Lyon 1, F-69622, Villeurbanne, France*
[2]*Department of Mechanical and Manufacturing Engineering, Parsons Building, Trinity College Dublin, Ireland*

(Received 8 March 2013; accepted 26 November 2013; published online 17 December 2013)

The integral momentum balance on a growing boiling bubble is investigated. All forces acting on the bubble are detailed, and the methods and assumptions used to calculate their integral resultants are discussed. The momentum balance computation is then performed using experimental data of bubbles growing on an artificial nucleation site in a controlled environment. The relative magnitude of each force component is compared, showing negligible dynamic forces, upwards forces composed mainly of the buoyancy and contact pressure components, and downwards forces being exclusively due to surface tension and adhesion. The difficulty encountered in measuring the apparent contact angle due to mirage effects has been highlighted; a new method, fitting numerically simulated bubble profile to the contour measurements has been proposed and used to correct the effects of refraction on the bubble profile determination. As all forces acting on the bubble were measured, it was possible to estimate the residuals of the momentum balance. Their small value validated both the expressions used for the forces and the methodology to evaluate their value.
 [http://dx.doi.org/10.1063/1.4844416]

I. INTRODUCTION

The understanding of bubble dynamics is of major interest for a wide range of situations, such as nucleate boiling, cavitation, gas desorption, injection of a gas into a fluid, etc. For this reason, much effort has been put forth over the last century towards obtaining a complete understanding of the forces acting on growing bubbles in order that they can be modelled accurately. Even though significant progress has been made, the research is on-going due to the complexity of the mechanisms involved.

The founding study on bubble dynamics was presented by Lord Rayleigh as early as in 1917.[1] Based on the momentum equation, he presented a model predicting the time evolution of a bubble size as a function of the internal pressure inside the bubble and of the reference pressure far from the bubble. Although very relevant for specific cases such as bubble cavitation and early stages of bubble growth after nucleation, this model is limited by its assumptions. The adiabatic bubble is spherical in an infinite, quiescent, incompressible, and non-viscous liquid. Also, the internal pressure is kept constant, and the surface tension is neglected.[2]

A major step towards the description of the forces acting on a bubble during nucleate boiling was achieved in the 1960s by Cochrane and Aydelott.[3,4] They developed Newton's second law for a bubble attached to a wall modelled as a rigid body, and enumerated analytically the different force component acting on such a body. They introduced the so-called *contact pressure* force accounting for the contact area between the bubble and a wall. They also introduced dynamic forces with the momentum variation and the drag force. This latter force component was, however, roughly modelled considering the bubble as a sphere. The inertia of the liquid was not expressed in the momentum balance, but only discussed in the analysis. The comparison between the model and

[a)]samuel.siedel@tcd.ie. Present address: Trinity College Dublin, Ireland.
[b)]Electronic mail: jocelyn.bonjour@insa-lyon.fr

experimental data was not possible or was too inaccurate due to the lack of controlled experiments involving single bubbles and the technical difficulties of measuring the relevant parameters during bubble growth at that time.

The 1990s were a prolific period for research concerning forces acting on growing bubbles. Klausner, Zeng, and Mei[5–7] refined the analytical expression of the force components acting on the bubble. They included an unsteady growth force to take into account the liquid inertia and the virtual added mass of the bubble, and they expressed a lift force to take into account the flow created by the wake of the preceding departed bubble. The bubble geometry was still idealized and was modelled as a truncated sphere for all force calculations, and no accurate experimental validation was available to validate the model. The contact pressure force being a function of the interface curvature at the base of the bubble, especially required a fine determination of the bubble shape, was simply considered as negligible at bubble departure. Buyevich and Webbon[8] enhanced the momentum balance modelling for the case of nucleate boiling bubbles by including bubble growth models in the determination of the dynamic forces. While predicting the momentum balance as a function of time during the whole bubble growth cycle, the growth models also employed geometric simplifications of the bubble shape, here considering them a perfect spherical segments. In addition, the growth models available were still in development and were not validated by accurate and controlled experiments.

The beginning of the current century is marked by new opportunities for performing controlled experimental studies thanks to the development of digital high-speed videography and image processing at low computational cost. Duhar and Colin[9–11] defined the new state-of-the-art by expressing analytically the momentum balance of an injected gas bubble in a viscous shear flow, and measuring the different force component from actual bubble images from controlled experiments. No shape assumption was made as the volume was integrated from the actual shape processed from the images. However, the simplified model of the relevant forces was still posed in terms of the equivalent bubble radius (i.e., the radius of a sphere of equivalent volume). This ostensibly assumed that the bubble was spherical from the point of view of the momentum balance, with the only unknown being the surface tension force. The efficacy of the model was then confirmed by solving the momentum balance expression for the contact angle and showing reasonable agreement with measured values, though only for the later stage of growth. Although this was a significant contribution, it must be noted that the model still idealized the bubble shape and this approach may mask the residual error of the momentum balance associated with measurement uncertainties and/or modelling assumptions.

More recently, Di Bari and Robinson[12] performed an experimental investigation on quasi-static gas injected bubble growth. By measuring the instantaneous gas pressure within the growing bubble and calculating the local bubble curvatures from the high speed video images, they were able to estimate the instantaneous liquid pressure field around the bubble. They then estimated the relevant vertical forces acting on the bubbles without making any assumptions about their shape. The correctness of their approach was confirmed by the forces balancing within experimental uncertainty. The Di Bari and Robinson[12] study highlights the point that idealizing the bubble shape to spherical geometries can influence some of the force calculations since they are inherently dependant on the bubble shape and the pressure distribution. This has been investigated by Lesage *et al.*[13] where a criterion has been posed which defines a threshold after which spherical idealizations are no longer valid.

With regard to bubble growth in nucleate pool boiling, the present authors emphasized in an earlier study[14] the need to avoid the reasoning in terms of equivalent radius, and to express instead the bubble characteristics as a function of the volume. The equivalent radius being proportional to the cubic root of the volume, it tends to hide the change of trends in the volume evolution. The bubble forces need to take into account the actual shape of the volume, and the equivalent radius approximation is often not sufficient when the local curvature radius is needed.

The present work aims to rigorously model the forces acting on a growing bubble during nucleate boiling and determine the expression of each forces with as few assumptions as possible. The resultant of the forces will then be computed using the actual shape of the bubble and measurements from the experimental images recorded. The full integral momentum balance will be computed, and the relative magnitude and influence of each term will be discussed. As each term will be calculated separately, the residual error in the momentum balance will be analysed.

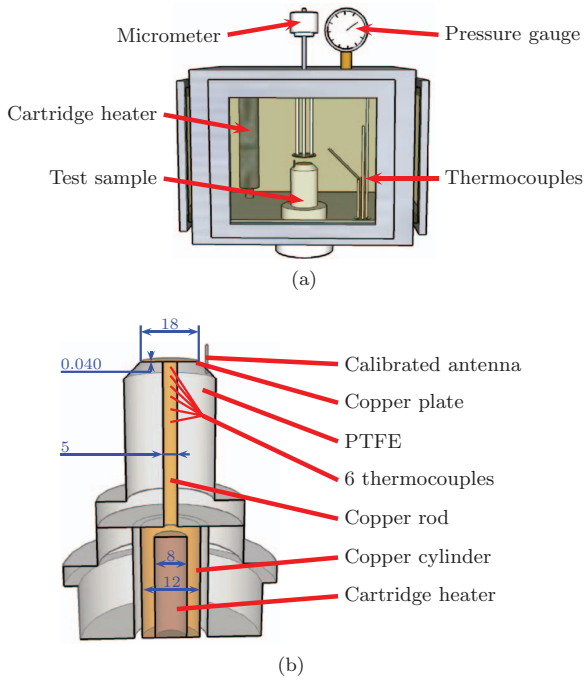

FIG. 1. Experimental facility. (a) Experimental vessel. (b) Test sample (length given in mm).

A. Experimental facility

The experimental apparatus, described by Siedel *et al.*[14,15] is shown in Figure 1(a). It consists of a sealed 250 mm × 250 mm × 180 mm vessel. To facilitate observation and photography within the vessel the vertical faces of the vessel were equipped with rectangular windows which were sealed to the main housing of the tank. Initially, the tank was evacuated and subsequently filled with 99% pure n-pentane. The free surface between the liquid and the vapour phases was at a height of approximately 220 mm from the base of the container. N-pentane was chosen as the working fluid as it has desirable properties; in particular it is non-toxic and has a relatively low boiling point of 35.7 °C.

A 350 W cartridge heater was immersed in the liquid pentane. Initially, this heater was utilized to over-pressurize the vessel to facilitate purging of dissolved gasses. Subsequent to this degassing, the immersion heater was employed to control the saturation temperature and pressure of the working fluid during testing. This heater was turned off for several minutes before each measurement in order to avoid convective flow rising from the heater. Four thermocouples were placed close to the test sample, in the vapour phase and in the upper and lower part of the liquid phase to monitor and control the saturation condition as well as to ensure temperature homogeneity within and between the liquid and the vapour phases.

Boiling took place atop the metered heater element illustrated in Figure 1(b). The heater element was situated in the centre of the vessel with the upper surface nominally 100 mm below the *vapour-liquid* free surface of the n-pentane, as depicted in Figure 1(a). The heater element was constructed from a 12 mm diameter solid copper cylinder. The lower end was machined to receive a 50 mm long 300 W cartridge heater with a diameter of 8 mm. In order to increase the axial heat flux as well as reduce the overall area of heat transfer at the exposed end of the heater element, the upper portion of the copper rod was reduced to a diameter of 5 mm. The upper portion of the copper pin section was equipped with six K-type thermocouples to monitor the axial temperature distribution. The entire heater element except the top surface was encased in PTFE in order to provide sufficient insulation to reduce radial heat losses.

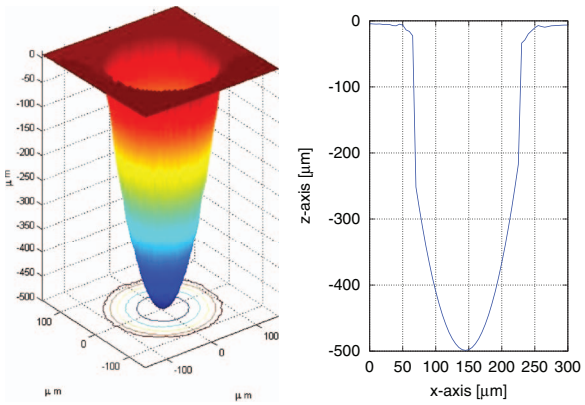

(a) (b)

FIG. 2. Nucleation site geometry. Colour shading refers to the depth. (a) 3D representation. (b) cross-section.

The boiling surface consisted of a 40 μm thin and 18 mm diameter copper sheet which was soldered to the top surface of the copper pin section. The plate was mirror-polished to reduce the number of potential nucleation sites on its surface. The plate was also thin enough to restrict radial heat flow to the extent that nucleation, and thus boiling, was avoided at its outer edge during tests.

A single artificial nucleation site was created by mechanical indentation at the centre of the plate. A tungsten carbide needle was constructed in-house and was positioned to be in intimate contact with the surface. It was then forced into the surface with its displacements accurately measured during the entire indentation process. The surface geometry of the site has been measured with a confocal white light microscope. As shown in Figure 2, the 500 μm deep cavity is generally parabolic and has a diameter of 180 μm. Approximately 30 K of superheat was required to initiate boiling at the artificial nucleation site. As a result of the care taken in the surface preparation and cleaning, boiling only occurred at this artificial nucleation site. At such high wall superheats, the nucleation site produces bubbles at such a rate as to generate a nearly continuous vapour column. As this boiling regime was not the focus of this investigation, the heat flux was reduced to the extent that the wall superheat was maintained between 1.5 and 8 K. This superheat range was high enough to generate discrete bubble events, albeit with very small waiting times, whilst being high enough to keep the nucleation site active.

As mentioned, boiling only took place in the middle of the vessel at the centre of the copper boiling surface. In order to capture the bubble growth dynamics with high enough temporal and spatial resolution, a Photron Fastcam 1024 PCI high speed digital camera was utilized. The bubble was illuminated with a diffuse backlight at a frequency of 200 kHz. The camera was capable of recording the bubble growth at image acquisition frequencies in the range of 1000–3000 fps.

The recorded images were processed by an in-house code using Matlab commercial software, in order to measure the characteristic geometric parameters of the bubbles. The raw contour of the bubble (see Figure 3(a)) was used to compute its volume by assuming the bubble as a stack of 1-pixel high vertical cylinders. Similarly, the height of the center of gravity was calculated as the weighted sum of the height of each cylinder. In order to measure the bubble local curvature, smoothing filters were employed on the raw bubble contour (see Figure 3(b), and see Siedel *et al.*[16] for a complete description of the image processing).

II. REVIEW ON THE FORCES ACTING ON THE BUBBLE

The forces acting on the bubble during its growth dictate the evolution of its shape and its motion, and therefore the conditions of departure from the surface. An analysis of the forces acting on the bubble during its growth has thus been performed in order to provide a better understanding of the bubble dynamics, and of the bubble detachment which plays a prominent role in boiling heat transfer.

(a) (b)

FIG. 3. Illustration of the successive steps of image processing. (a) Determination of the bubble contour. (b) Bubble local curvature.

The control volume used for the force analysis applied to a bubble (Fig. 4(a)) is described in Fig. 4(b). The bubble contour is obtained by image processing from the experimental images. The control volume is defined by the bubble's volume excluding the volume of the nucleation site beneath the surface. The boundaries of the control volume are as follows:

The liquid side of the liquid-vapour interface: Between the vapour bubble and the surrounding liquid.

The contact line (CL, Fig. 4(c)): Between the vapour, the liquid and the solid phases. In our experiments, the contact line does not move during bubble growth, resulting in a constant contact line length.

The vapour-vapour interface: Between the bubble and the nucleation site. This boundary has a fixed area as the contact line does not move.

A specific subdivision of the control volume will be used for the resolution of the momentum equation. The different volumes, surfaces, and lines involved are described in Fig. 4(c).

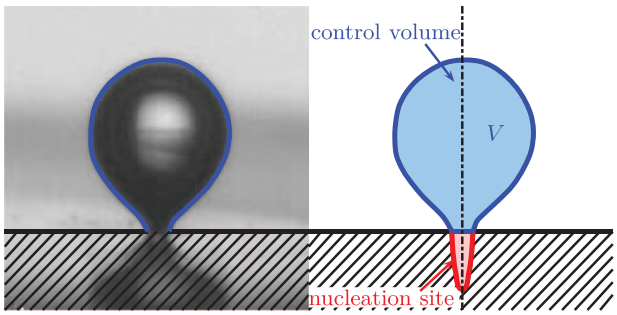

(a) (b)

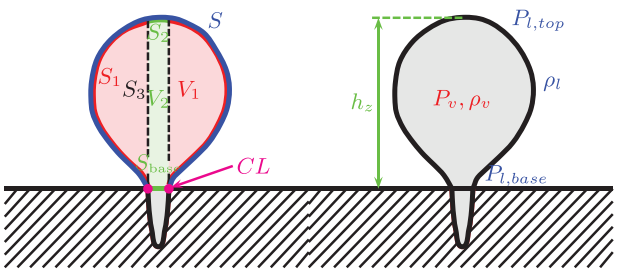

(c) (d)

FIG. 4. Schematic of the control volume for the momentum balance. (a) Image with bubble contour. (b) Schematic of the control volume. (c) Volumes, surfaces, and lines involved. (d) Thermodynamic variables involved.

The momentum conservation law states that within a control volume, the variation of momentum is equal to the sum of the external forces applied to this control volume. It is necessary to emphasize the fact that the momentum variation is an integral value. It provides information about a change of mass of the control volume or a motion of its center of gravity, but does not indicate a change of shape as long as the center of gravity remains at the same location.

The formulation of the momentum equation strongly depends on the hypotheses chosen and on the forces taken into account. Indeed, a full resolution of the most general momentum equation would require exact knowledge of the instantaneous velocity field, temperature field, and local rate of heat transfer, which is not possible to know with certainty.

The expressions for the forces are compiled from various publications among which are Zeng *et al.*,[5] Kandlikar and Stumm,[17] Duhar and Colin,[9,10] Buyevich and Webbon,[8] Chen *et al.*,[18] and Ginet.[19] The integral form of the momentum equation considered is

$$\frac{\mathrm{d}}{\mathrm{d}t}\iiint_V \rho_v \overrightarrow{u_v}\ \mathrm{d}V = \overrightarrow{F}_{LI} + \overrightarrow{F}_{buoy} + \overrightarrow{F}_{\sigma} \tag{1}$$

with $\overrightarrow{F}_{LI}$, $\overrightarrow{F}_{buoy}$, and $\overrightarrow{F}_{\sigma}$, respectively, are the resultant of the liquid inertia, the buoyancy, and surface tension and adhesion forces. All these forces are detailed in Subsections II A–II E. Some forces have been neglected, such as the viscous stress due to thermocapillary flow or to the motion of the liquid induced by the bubble or by the preceding bubble. The assumptions about these forces are also discussed in Subsections II A–II E.

A. Momentum variation

The derivative with time of the momentum can be considered as the resultant of the static and dynamic forces. As the momentum variation is analogous to a force, it is chosen for the sake of a better readability to refer to it as $\overrightarrow{F}_{mom}$:

$$\overrightarrow{F}_{mom} = \frac{\mathrm{d}}{\mathrm{d}t}\iiint_V \rho_v \overrightarrow{u}_v\ \mathrm{d}V. \tag{2}$$

Considering a symmetrical gain of mass of the bubble (see the Appendix concerning this assumption), the integration of the velocity vector is equal to the velocity of the center of gravity $\overrightarrow{u}_{cg}$.

$$\overrightarrow{F}_{mom} = \frac{\mathrm{d}}{\mathrm{d}t}\left(\rho_v \overrightarrow{u}_{cg} \times \iiint_V \mathrm{d}V\right) \tag{3}$$

$$= \frac{\mathrm{d}}{\mathrm{d}t}\left(\rho_v \overrightarrow{u}_{cg} \times V\right) \tag{4}$$

$$= \rho_v \overrightarrow{u}_{cg}\frac{\mathrm{d}V}{\mathrm{d}t} + \rho_v V\frac{\mathrm{d}\overrightarrow{u}_{cg}}{\mathrm{d}t}. \tag{5}$$

Considering h_{cg} as the height of the center of gravity, $\overrightarrow{k}$ the unit vertical vector in the upward direction, and assuming the motion of the center of gravity being vertical:

$$\overrightarrow{F}_{mom} = \rho_v \frac{\mathrm{d}h_{cg}}{\mathrm{d}t}\frac{\mathrm{d}V}{\mathrm{d}t}\overrightarrow{k} + \rho_v V\frac{\mathrm{d}^2 h_{cg}}{\mathrm{d}t^2}\overrightarrow{k}. \tag{6}$$

As $h_{cg}(t)$ and $V(t)$ are measured from the recorded images, the resultant of the momentum derivative with time can be computed.

B. Liquid inertia and added mass force

The liquid inertia and added mass force is the liquid reaction to its acceleration caused by the motion of the interface. Its expression is similar to the momentum variation except for two differences:

- The density considered is now the liquid density.
- Each term is weighted by a coefficient usually referred to as *added mass coefficient*:

$$\overrightarrow{F}_{LI} = K_1 \rho_l \frac{\mathrm{d}h_{cg}}{\mathrm{d}t} \frac{\mathrm{d}V}{\mathrm{d}t} \overrightarrow{k} + K_2 \rho_l V \frac{\mathrm{d}^2 h_{cg}}{\mathrm{d}t^2} \overrightarrow{k}. \tag{7}$$

The value of the added mass coefficients depends on the shape of the bubble and on its proximity to the wall. In the present case, the exact value of each coefficient varies with time and cannot be easily estimated. The coefficients can however be bounded by extremum values obtained for simple cases by numerical simulation. Duhar[9] and Magnaudet *et al.*[20] indicate coefficients both equal to 0.5 for the case of a spherical bubble growing in an infinite liquid. For the case of a hemisherical bubble growing on a wall, Klausner *et al.*[6] and Legendre *et al.*[21] give $K_1 = 2$ and $K_2 = 4$. The actual coefficients for the present experimental bubble growth are considered to be within this range.

It can be noted that the difference between the momentum force and the liquid inertia force is of the order of the density ratio, ρ_l/ρ_v. This ratio is usually high, and is equal to 206 in the specific case of this study. The momentum force can thus be neglected in most cases. This inertia argument was also stated by Robinson and Judd.[22]

C. Buoyancy

The buoyancy force can be considered as the resultant of the hydrostatic pressure forces on the bubble surface. It is sometimes considered as only the resultant of the liquid pressure forces, and sometimes also includes the resultant of the vapour pressure forces. Here, the second approach is retained. This force is due to the vertical pressure gradient caused by gravity. The pressures involved are the hydrostatic liquid pressure on the outward surface S, the hydrostatic vapour pressure on the inward surface S and the vapour pressure on both sides of the surface S_{base} (see Figure 4(c)).

Following the reasoning introduced by Cochrane *et al.*,[4] and considering homogeneous liquid and vapour densities, the buoyancy can be broken down into the three following terms:

$$\overrightarrow{F}_{buoy,1} = (\rho_l - \rho_v) V g \overrightarrow{k}, \tag{8}$$

$$\overrightarrow{F}_{buoy,2} = -(\rho_l - \rho_v) V_2 g \overrightarrow{k}, \tag{9}$$

$$\overrightarrow{F}_{buoy,3} = \frac{2\sigma}{R} S_{base} \overrightarrow{k}, \tag{10}$$

with $\overrightarrow{F}_{buoy,1}$ being the buoyancy force as if the bubble was fully immersed in the liquid, $\overrightarrow{F}_{buoy,2}$ being a first correction term on the buoyancy to take into account only the part of the bubble which is located with liquid below and above, and $\overrightarrow{F}_{buoy,3}$ being a second correction term on the buoyancy (sometimes referred to as *contact pressure*) which considers the pressure difference across the interface area located above the nucleation site.

D. Triple line surface tension and adhesion forces

The effects of the forces involved at the contact area between the 3 different phases are very complex. The geometry of the triple line and the forces applied at this location are governed by both the surface tension between the liquid and vapour phases and the wettability of the liquid over the solid surface. The wettability, usually characterized by a contact angle θ, results from the

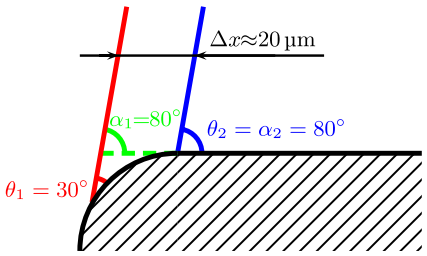

FIG. 5. Evolution of the contact angle θ and of the angle α for a small change in the triple line location close to the nucleation site edge.

competition of molecular and capillary forces (see de Gennes *et al.*,[23] p. 24). The resultant of the triple line forces, commonly named simply the "surface tension force," is expressed as follows:

$$F_\sigma . \overrightarrow{k} = \int_{CL} \sigma \overrightarrow{t}\ \mathrm{d}l \tag{11}$$

with $\overrightarrow{t}$ the unit vector tangential to the interface in the meridian plane and at the contact line.

If the bubble or at least the base of the bubble is axisymmetric, this term can be expressed as follows:

$$F_\sigma = -2\pi R_{base} \sigma \sin\alpha \tag{12}$$

with $2\pi R_{base}$ being the perimeter of the triple line of radius R_{base}, and α being the angle between the interface at the triple line and the horizontal plane. This angle is defined in the liquid phase.

As most models describe bubble growth on a plane surface, α is generally simply taken as the contact angle θ. However, in the case of this study, these angles may be very different. As an illustration, Fig. 5 shows schematically two different positions of the triple line which, as viewed at the scale of the experiments – and in spite of optical magnification systems –, are both located on the rim of the nucleation site. A large variation on the contact angle θ is observed for a small displacement of the triple line. Yet, the angle α is the same in both cases and is equal to θ_2.

In order to calculate the adhesion force, the value of the contact angle α is measured from the processing of the images.

E. Neglected forces

All the forces previously taken into account consider either a static fluid (buoyancy) or a fluid motion induced by the bubble (momentum variation and liquid inertia). However, several other causes of liquid motion may be identified. Any liquid motion affects the momentum balance by causing a shear viscous stress at the bubble interface. These causes of liquid motion may be classified as follows:

- The surface tension is a *liquid-vapour* property of the fluid that describes the force equilibrium at the interface. This property varies with several parameters:
  - Surface tension gradients arise due to chemical or concentration gradients at the interface. This is the case when boiling mixtures or when using surfactants. None of these cases are involved in this experimental study as particular care has been given to employ a perfectly pure pentane in the experiments.
  - Surface tension gradients may also be caused by temperature gradients. Surface tension is indeed varying with temperature, and is generally decreasing with an increasing temperature. This is the case for pentane. In saturated condition at $P = 1$ bar, $\frac{\mathrm{d}\sigma}{\mathrm{d}T} \approx -9.98 \times 10^{-5} \mathrm{N\,m^{-1}\,K^{-1}}$.

  Similarly to curvature gradients, surface tension gradients can be the driving force for fluid motion. This phenomenon is often referred to as the Marangoni effect, or as the thermocapillary

effect when the surface tension gradient is due to a temperature gradient, as detailed by Petrovic *et al.*[24]

Marangoni flows affect the momentum balance by causing a shear viscous stress at the interface. The liquid viscosity being much larger than that of vapour, the viscous stress is mostly applied on the liquid side of the interface. Marangoni flows are known to play a prominent role in micro-gravity conditions, in the case of downward facing bubbles, in the case of highly subcooled boiling, in the presence of surfactant or when boiling fluid mixtures.

As detailed by Marek and Straub,[25] no thermocapillary convection occurs in saturated boiling of pure liquids, as the interface of the bubbles are isothermal at the saturation temperature of the vapour pressure. Temperature gradients may occur due to the presence of non-condensible gases, especially with non-degassed water, and in the case of subcooled boiling due to condensation on the dome of the bubble.

In the present momentum balance analysis, pure and degassed pentane is boiled at saturation. The forces due to the viscous stress induced by potential thermocapillary effects will thus be neglected.

- A shear lift force is applied on the bubble due to the convective motion of the surrounding liquid. As described by Siedel *et al.*,[15] the superheated liquid is naturally rising and forming a plume at the center of the heated plate. The viscous liquid flow shears the bubble and the resultant viscous force applied on the bubble is in the flow direction. This force is similar to that of a convective flow (see Mei and Klausner[7]), except that convective flows are usually tangential to the heated wall. However, the liquid velocities implied in natural convection are at least an order of magnitude below the flow velocities of a shear flow: as depicted by Siedel *et al.*,[15] velocities in the plume are of the order of 5–10 $\mathrm{mm\,s^{-1}}$. This shear flow forces can thus be neglected.
- The inertia of the liquid moved by the bubble is taken into account. However, viscous stress is also caused by the motion of the bubble itself. The *liquid-vapour* interface is moving due to bubble translation and expansion. Similar to the shear lift force due to convective liquid motion, the velocities are very low. In accordance with the literature studies on forces applied on a growing bubble,[5,8,9,17–19] this force is neglected.
- A rising bubble is drawing liquid in its wake. This flow field can impact the next growing bubble if the latter is close enough. The resultant of this force would be a vertical lift force that tends to detach the new bubble from the wall. Zeng *et al.*[5] have established an approximate expression of this force. For a spherical bubble of radius R rising over a hemispherical bubble of identical radius R at a velocity of u, L being the distance between the center of each bubble, the resultant of the lift force applied on the hemi-spherical bubble is

$$F_{lift} = \frac{75}{16}\rho_l u^2 R^2 \left(\frac{R}{L}\right)^8. \tag{13}$$

It is noticeable that the force is proportional to L^{-8}. This indicates that the force is non-negligible only when both bubbles are very close to each other. This was observed in this study for moderate to high wall superheats when the new growing bubble almost *reached* the preceding bubble at the beginning of its growth (see Siedel *et al.*[14] for more details about the oscillations caused on a bubble by the previous bubble). This phenomenon is a particular case encountered, as the lift force amplitude decreases under 0.1 μN when distance between the bubbles reaches 2 mm, using the order of magnitude of the experiment concerning the rising velocity and the bubble size. Such a distance is reached in the first 10 ms after departure of the first bubble. Therefore, this force will not be taken into account in the present momentum balance.

III. COMPUTATION OF THE MOMENTUM BALANCE

The integral form of the momentum balance is computed at each time step of bubble growth, for a wall superheat of 2.1 K. The same computation will then be performed for a wall superheat of

4.7 K, and the results will be compared. The following momentum equation is solved

$$\frac{\mathrm{d}}{\mathrm{d}t}\iiint_V \rho_v \overrightarrow{u_v}\ \mathrm{d}V = \overrightarrow{F}_{LI} + \overrightarrow{F}_{buoy,1} + \overrightarrow{F}_{buoy,2} + \overrightarrow{F}_{buoy,3} + \overrightarrow{F}_{\sigma} + \overrightarrow{\varepsilon}_{res} \tag{14}$$

with, as detailed previously:

- $\overrightarrow{F}_{mom} = \frac{\mathrm{d}}{\mathrm{d}t}\iiint_V \rho_v \overrightarrow{u_v}\ \mathrm{d}V$ the momentum variation of the bubble,
- $\overrightarrow{F}_{LI}$ the resultant of the inertia forces of the liquid moved by the bubble,
- $\overrightarrow{F}_{buoy,1}$, $\overrightarrow{F}_{buoy,2}$, and $\overrightarrow{F}_{buoy,3}$ the buoyancy terms,
- $\overrightarrow{F}_{\sigma}$ the resultant of the triple line surface tension and adhesion forces, and
- $\overrightarrow{\varepsilon}_{res}$ the residual error on the determination of the momentum balance, which can be due to measurement uncertainty, to approximations in the calculation and to non-negligible forces that were not taken into account in this momentum balance.

For the sake of readability, only the norm of the forces will be computed. As the problem considered presents an axial symmetry, the norm will be expressed in the vertical direction and upwards:

$$F = \overrightarrow{F} \cdot \overrightarrow{k}\,. \tag{15}$$

The forces considered are in fact the resultant of pressures or of linear forces integrated over a surface or a contour. Throughout section III, the term *resultant* will refer either to the integrated vectorial force considered or to its norm.

A. Computation of the angle α and of the adhesion forces

The angle α is the angle between the interface at the triple line and the horizontal plane. This angle is defined in the liquid phase. The value is obtained using the image processing method described in another publication by the same authors.[16]

The smoothed interface of a sample bubble at a wall superheat of 2.1 K and at $t^* = 0.5$ is shown in Figure 6. The angle α is defined at the base of the bubble, between the wall and the interface of the bubble, as depicted in Figure 6. α is calculated from the two data points of the smoothed interface that are located the closest to the wall.

The angle α is measured at different time steps during bubble growth, as shown in Figure 7(a). It should be noticed that for $t^* < 0.05$, it is not possible to correctly capture the bubble contour due to the small size of the bubble. The angle α is thus not measured at the beginning of the growth cycle.

The measured angles obtained are then fitted with a polynomial function (see Figure 7(a)). A 6th order polynomial was used in order to capture the fact that the angle decreases rapidly at the

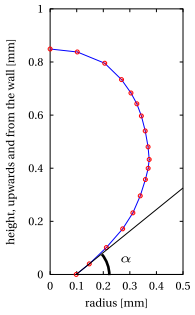

FIG. 6. Smoothed interface of a bubble at a wall superheat of 2.1 K and at $t^* = 0.5$.

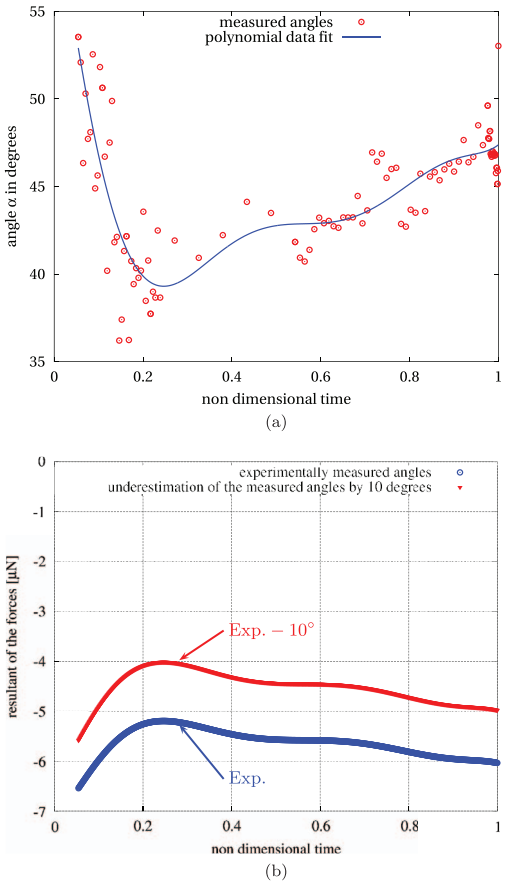

FIG. 7. Computation of the resultant of the triple line surface tension and adhesion forces for a growing bubble at a wall superheat of 2.1 K. (a) Evolution of angle α. (b) Resultant of the adhesion forces acting on a bubble, using the measured angle α and an underestimation of the angle by 10°.

beginning, reaches a minimum value and then increases slowly. The small oscillations observed are inherent to the polynomial fitting and do not represent the trends of the experimental data. This function is used to compute the adhesion force acting on the bubble during its growth. This force is expressed by Eq. (12).

The base diameter and the surface tension being taken as constant with $R_{base} = 90\ \mu$m and $\sigma = 0.014269\ \mathrm{N\,m^{-1}}$, the resultant of the adhesion forces is calculated and plotted in Figure 7(b).

As an illustration of the sensitivity of this force to the measurement of α, Figure 7(b) shows its evolution using the measured value of α and an arbitrary adjusted value of α decreased by 10°. Such a difference in the angle results in an offset in the force calculation by about 1 μN, which is significant. An accurate determination of α is thus needed, and will be discussed in Sec. III F.

B. Computation of the momentum variation

For the computation of the momentum balance, the exact formulation of the momentum variation is expressed as follows:

$$\overrightarrow{F}_{mom} = \rho_v \frac{\mathrm{d}h_{cg}}{\mathrm{d}t}\frac{\mathrm{d}V}{\mathrm{d}t}\overrightarrow{k} + \rho_v V \frac{\mathrm{d}^2 h_{cg}}{\mathrm{d}t^2}\overrightarrow{k} \tag{16}$$

with $\overrightarrow{k}$ being the unit vertical vector in the upward direction and h_{cg} being the height of the center of gravity.

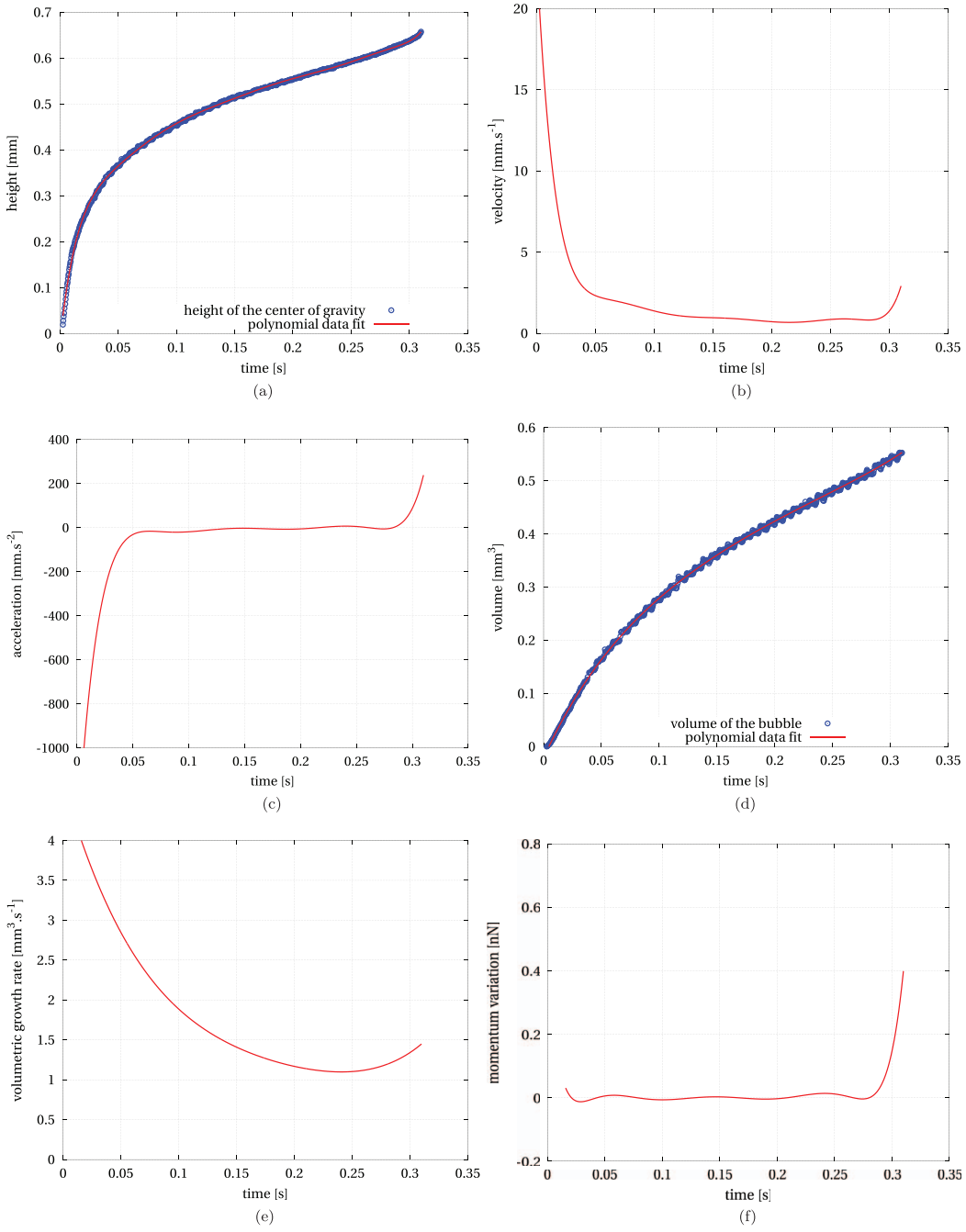

FIG. 8. Computation of the momentum variation of a growing bubble at a wall superheat of 2.1 K. (a) Height of the center of gravity. (b) First time derivative of the height of the center of gravity. (c) Second time derivative of the height of the center of gravity. (d) Volume of a bubble. (e) Volumetric growth rate. (f) Momentum variation.

The height of the center of gravity is measured through the processing of the recorded images and shown in Fig. 8(a). The measured height is fitted with an appropriate polynomial function. Its first and second derivatives are computed, and are shown in Figs. 8(b) and 8(c). Using the same approach, the volumetric growth is fitted with an appropriate polynomial function (see Fig. 8(d)). The first time derivative of the function approximates the volumetric growth rate (see Fig. 8(e)).

The momentum variation is calculated using the thermodynamic properties of pentane, the first and second time derivative of the height of the center of gravity, the volume of the bubble and its

first time derivative. The momentum variation obtained is shown in Fig. 8(f). It is computed only for $t^* > 0.05$ as the uncertainty is very high at the beginning of growth and other forces cannot be computed for $t^* < 0.05$.

A sensitivity analysis has been performed concerning the order of the polynomial functions used. It has been concluded that a 7th and 5th order polynomial functions are the most appropriate in order to fully capture the different phases of the momentum variation. At the beginning of the growth, its amplitude is positive and decreases due to the first term of the momentum variation: both the velocity of the centre of gravity and the volumetric growth rate are positive and relatively high, but decreasing. During most of the growth, the momentum variation is very small. Just before bubble departure, its amplitude increases quickly due to the second term of the momentum variation: the centre of gravity of the large bubble accelerates suddenly.

These trends were not possible to capture properly with lower order polynomials. Unfortunately, small oscillations inherent to the higher order polynomial functions can be observed, and do not necessarily represent the trend of the experimental data.

It can be noticed from Fig. 8(f) that the momentum variation is lower than 0.4 nN. This value is negligible compared to the magnitude of the other forces, as it was already expected by comparison to the liquid inertia force.

It should also be noticed that the determination of the first and second derivative of measured data causes high uncertainty. This uncertainty does not impact the momentum balance as the momentum variation is negligible.

C. Computation of the liquid inertia forces

The liquid inertia force is the resultant of the forces induced by the displacement of liquid due to the bubble motion and growth. Similarly to the momentum variation, the resultant of the liquid inertia forces can be expressed as a function of the thermodynamic properties of pentane, the first and second time derivatives of the height of the center of gravity, the volume of the bubble and its first time derivative and two added mass coefficients:

$$\vec{F}_{LI} = K_1 \rho_l \frac{\mathrm{d}h_{cg}}{\mathrm{d}t} \frac{\mathrm{d}V}{\mathrm{d}t} \vec{k} + K_2 \rho_l V \frac{\mathrm{d}^2 h_{cg}}{\mathrm{d}t^2} \vec{k}. \tag{17}$$

The value of the added mass coefficients is not known but considered as bounded by $K_1 = K_2 = 0.5$ and $K_1 = 2$ and $K_2 = 4$ (see Sec. II B).

Using the results of the computation of the momentum variation, the resultant of the liquid inertia forces is computed and plotted in Fig. 9 using the two previously mentioned sets of added mass coefficients. Its value is always below 0.4 μN. This is an order of magnitude below other forces such as the buoyancy force and the adhesion forces, calculated in this section. This was expected as the bubble shape and volume at departure were similar for any wall superheat whereas the growth rate was varying, as mentioned by Siedel *et al.*[14]

In order to verify if the liquid inertia forces are negligible when calculating the momentum balance, the highest added mass coefficients will be used.

D. Computation of the buoyancy forces

The two first buoyancy terms are respectively proportional to the total volume V of the bubble and to the volume V_2 located above the nucleation site. These volumes are obtained by processing the recorded images, and shown in Figure 10.

The third buoyancy term considered takes into account the pressure difference through the interface located above the nucleation site. For the computation of this term, the Young-Laplace equation is used in order to calculate the pressure difference from the curvature of the bubble at its apex. This buoyancy term is expressed as follows:

$$\vec{F}_{buoy,3} = \frac{2\sigma}{R} S_{base} \vec{k} \tag{18}$$

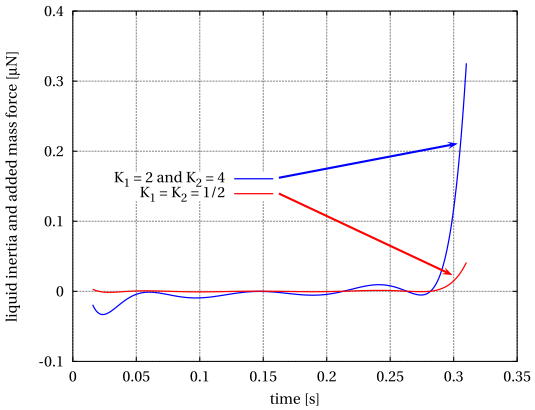

FIG. 9. Resultant of the liquid inertia forces acting on a growing bubble at a wall superheat of 2.1 K, using two different sets of added mass coefficients.

with S_{base} being the surface of the base of the bubble, as described in Fig. 4(c) and R being the radius of curvature at the apex of the bubble. As it is located on the axis of symmetry of the bubble, both main radii of curvature are equal. The curvature is taken as homogeneous on the surface considered, which is consistent with curvature measurements shown by Siedel *et al.*[16]

As the total curvature C is measured from these recorded images, the third buoyancy term can also be expressed as follows:

$$\overrightarrow{F}_{buoy,3} = \sigma C_{tip} S_{base} \overrightarrow{k}, \tag{19}$$

where C_{tip} being the curvature at the apex of the bubble. The evolution of the curvature at the apex is shown in Fig. 11(a). C_{tip} is of course proportional to the vapour pressure within the bubble through the surface tension.

For the same reasons discussed earlier, it is not possible to correctly capture the bubble contour for $t^* < 0.05$. The curvature is thus not measured at the beginning of the growth. Here again, the measured curvature data are fitted with an appropriate polynomial function which is then used to calculate the resultant of the third buoyancy term (see Fig. 11(b)).

E. Results of the momentum balance

Figure 12(a) shows the evolution of all the forces considered during a bubble growth event with a wall superheat of 2.1 K. Similar results were obtained at a wall superheat of 4.7 K and are shown in Fig. 12(b). As explained earlier, the momentum balance has been computed only for $t^* > 0.05$.

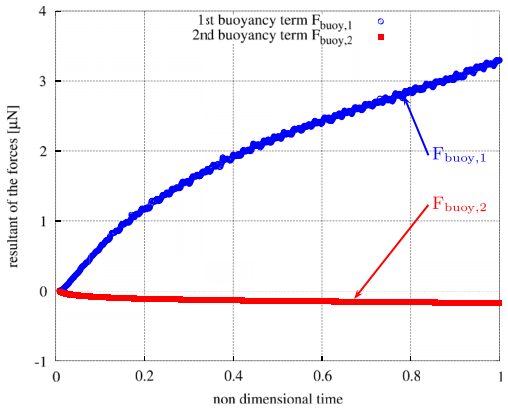

FIG. 10. Two first buoyancy terms of a growing bubble at a wall superheat of 2.1 K.

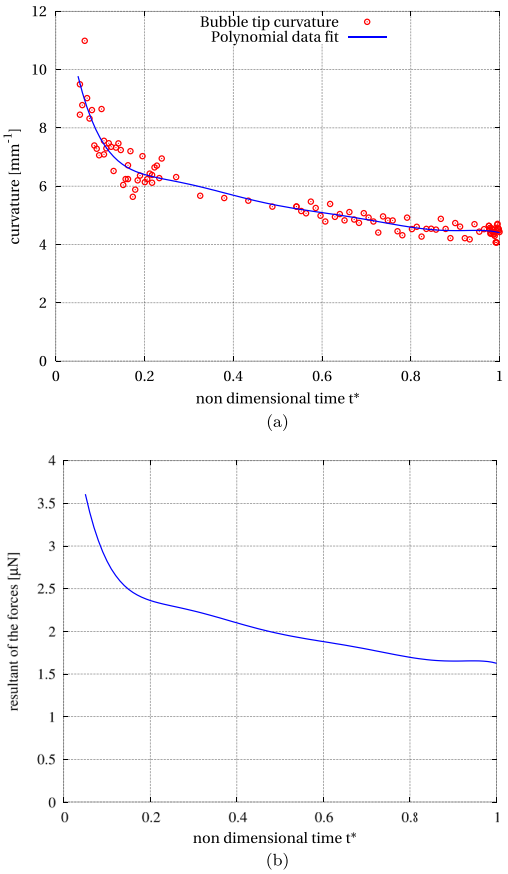

FIG. 11. Computation of the third buoyancy term of a growing bubble at a wall superheat of 2.1 K. (a) Curvature at the apex. (b) Resultant of the third buoyancy term acting.

As can be seen in Figure 12(a), the momentum variation is negligible. As $\rho_l \gg \rho_v$, the momentum variation is very small compared to the liquid inertia.

The liquid inertia force is also negligible. It was also expected because no notable influence of the wall superheat was observed on the bubble evolution and departure. All dynamic forces are thus negligible compared to the static forces.

The separation of buoyancy into three different terms highlights the role of each mechanism. The buoyancy due to the vapour volume $F_{buoy,1}$ corrected by $F_{buoy,2}$ increases monotonically, until being the dominant force that tends to detach the bubble. The so-called *contact pressure* term $F_{buoy,3}$ begins very high. Indeed, the curvature at the tip of the bubble is very low when the bubble is small, leading to a high vapour pressure at the beginning of the growth. This buoyancy term then decreases until being about half of the first buoyancy term.

The triple line surface tension and adhesion forces are the only forces keeping the bubble attached to the heated wall. These forces depend on the angle α which varies from 40° to 55°.

A non-negligible residual error is calculated for the entire bubble lifetime. Its value is close to that of the third buoyancy term (contact pressure), and it is directed upwards. This error might be due to uncertainties in the computation of the forces, especially the triple line adhesion force. As it has been detailed previously, the triple line adhesion force is very sensitive to the measurement of the angle α. Numerical simulation of the static equilibrium interface has thus been developed in order to verify the measurements of the contact angle.

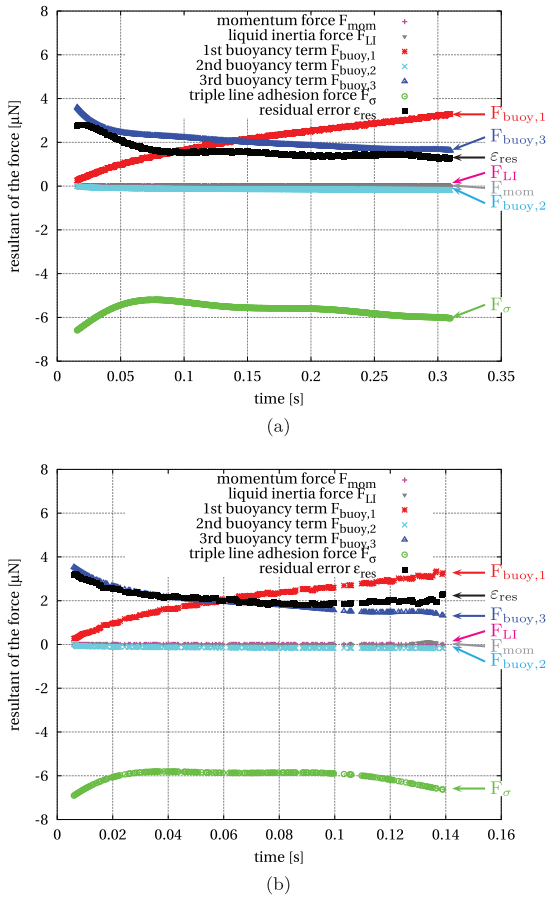

FIG. 12. Momentum balance for two growing bubbles, at a wall superheat of $\Delta T_W \approx 2.1$ K (a) and of $\Delta T_W \approx 4.7$ K (b). (a) Wall superheat of $\Delta T_W = 2.1$ K. (b) Wall superheat of $\Delta T_W = 4.7$ K.

F. Correction of the apparent contact angle

An error in the determination of α is possible for the following reason: with the strong temperature gradients caused by the heated surface and by phase change at the triple line, the location where α is measured is the zone of the recorded images which can be the most distorted by mirage effects, as first cautioned by Cooper.[26] If the occurrence of mirage effect was not completely avoided in the present experiments, it would result in an over-estimation of the angle α. In order to reduce mirage effects, the recording angle was slightly modified to allow a 3° angle with the horizontal plane. Consequently, the measurement of α from the images over-estimate the real angle because of both the modification of the recording direction and the possible remaining mirage effects.

Numerical simulation of the static bubble shape has been developed by solving geometrically the Young-Laplace equation for an axisymmetric interface. This equation expresses the mechanical equilibrium at each point of the interface as a balance between the pressure difference across the interface and the stress in the interface, formally the product of the surface tension and the curvature. If the bubble is axisymmetric in the vertical direction and the pressure gradients in each phase are purely hydrostatic, the Laplace-Young equation can be expressed as follows:

$$\sigma\left(\frac{1}{R_1}+\frac{1}{R_2}\right)=\frac{2\sigma}{R_0}-g\,(\rho_l-\rho_v)\,(z-z_0) \tag{20}$$

with R_1 and R_2 being two main radii of curvature, R_0 being the radius of curvature at the apex, z being the height in the vertical direction upwards, z_0 being the height of the apex and g being the terrestrial gravity acceleration. The thermodynamic properties of pentane are used for solving this

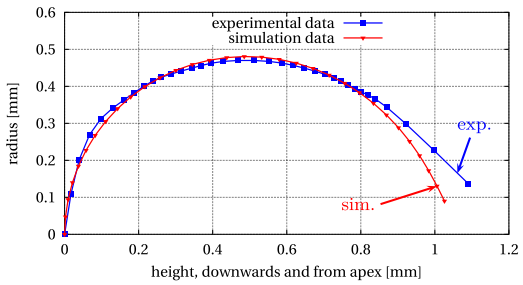

FIG. 13. Comparison between the bubble contour obtained by image processing from experimental data (squares, blue) and obtained by simulation (triangles, red) for a 0.487 mm^3 pentane bubble on a 90 μm radius orifice.

equation. For the case of an axisymmetric bubble, only one solution exists for each given set of apex radius of curvature R_0 and total height of the bubble.

An iterative method has been developed in order to generate unique profiles using as input parameters the volume of the bubble and the radius of its base. In order to do this, a first profile is computed numerically using a geometrical approach described by Gentes *et al.*[27] The radius of curvature of this first iteration is chosen arbitrarily. The profile, starting from the apex, is initially almost spherical, and deviates from the spherical shape as the distance from the apex increases. When the radius of the profile decreases until reaching the target radius of the base of the bubble, the profile is cut. The volume of the generated bubble is integrated by summing the conical frustums. The volume of the generated bubble is compared to the target volume. The radius of curvature of the apex is modified accordingly for a new iteration of the whole process. The iterations are stopped when the generated volume converges to the target volume.

Figure 13 shows the comparison between the contour obtained by image processing and by simulation for a 0.487 mm^3 bubble. Both profiles coincide on the upper 80% of the bubble. However, a non-negligible difference is observed close to the base of the bubble, where the temperature gradients and thus the mirage effects are strongest. It is assumed that the simulated profile is a more accurate representation of the bubble profile near the bubble base compared with the measured profile.

Using a wrong profile at the base of the bubble has several consequences on the results of the force analysis provided previously. The total bubble height is over-estimated as the nucleation is *seen* as if it were lower. The volume of the bubble is also slightly over-estimated, but this effect remains small as the radius near the base is small. However, the main consequence is an over-estimation of the apparent contact angle which can show an offset up to 20° compared to reality. As discussed earlier and illustrated in Fig. 7(b), this error will cause the adhesion force to be approximated incorrectly.

The relationship between the apparent contact angle and the volume of the bubble has been simulated and is shown in Fig. 14. The simulated contact angles are about 20° lower than the measured ones, as compared with Fig. 7(a).

G. Correction of the momentum balance

The momentum balance can be computed again using the simulated values of the apparent contact angle. At each time step of the growth, the volume is measured from the recorded images, and the apparent contact angle is estimated using the relationship between the contact angle and the bubble volume presented in Fig. 14. The momentum balance computations for bubbles with wall superheat conditions of 2.1 K and 4.7 K are plotted, respectively, in Figures 15(a) and 15(b).

As the apparent contact angle is now smaller, the absolute value of the triple line adhesion force F_σ (which is proportional to the sine of the angle) is also smaller by 30%–50%. As a consequence, the imbalance represented by the residual error term ε_{res} is now much lower.

The imbalance ε_{res} is now directed downwards, and its absolute order of magnitude is now around 0.5 μN. This small error may be due to uncertainty in the value of the surface tension for the simulation of the bubble profile and for the determination of the contact angle. Indeed, as noted previously, the surface tension between the liquid and vapour phases of pentane is a thermodynamic

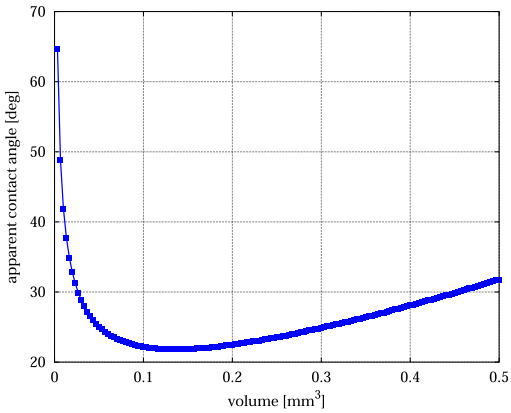

FIG. 14. Simulation of the apparent contact angle evolution with the bubble volume, with the physical and geometrical conditions of the experiment.

property that depends on the temperature. The value used for the simulation was taken at the saturation temperature of the bulk liquid ($T_{sat} \approx 35.9\ ^{\circ}$C at P=1 bar); however, the liquid at the vicinity of the boiling surface is superheated within the thermal boundary layer near the surface. For example, for a wall superheat of 4.7 K, the surface tension is decreased by about 3%. A decrease of surface tension tends to increase the apparent contact angle, and may increase the absolute value

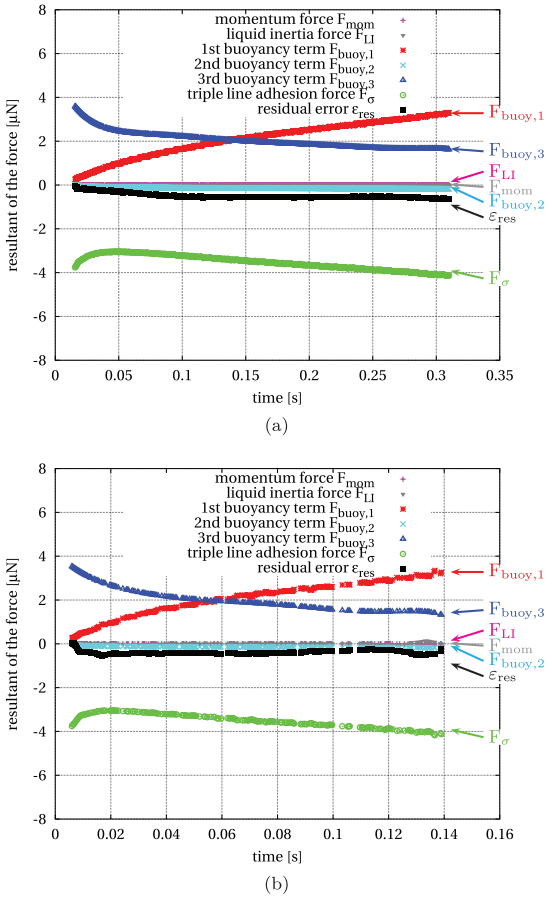

FIG. 15. Momentum balance for two growing bubbles, at a wall superheat of $\Delta T_W \approx 2.1$ K (a) and of $\Delta T_W \approx 4.7$ K (b), using simulated values of the contact angle for the determination of the triple line adhesion force. (a) Wall superheat of $\Delta T_W = 2.1$ K. (b) Wall superheat of $\Delta T_W = 4.7$ K.

of the triple line adhesion forces F_σ. However, in order to take into account the surface tension variations in the bubble profile simulations, the knowledge of the temperature profile along the interface is needed, which is not available from the current measurements.

IV. CONCLUSIONS

This work presents an experimental and theoretical analysis of the forces acting on a single bubble growing on an artificial nucleation site, and the full computation of the momentum balance during the entire bubble lifetime. After defining the control domain of the bubble, all static and dynamic forces were reviewed. The exact expression of the momentum variation was establish as a function of the volumetric evolution and of the height of the center of gravity. A similar expression was established concerning the resultant of the liquid inertia forces, balanced by two added mass coefficients that are unknown *a priori*. The buoyancy force was developed, taking into account the presence of the contact area. The surface tension and adhesion forces acting on the triple line were analysed and their resultant was expressed in terms of measurable variables. Eventually, the other dynamic forces were detailed. The assumptions leading to neglecting these forces were stated.

In a second part, all the forces considered in the momentum balance were computed from the experimental images recorded. The necessary assumptions, the image processing, and the force calculations were detailed, and the uncertainty on the results were discussed.

The dynamic forces computed were negligible compared to the other forces involved. For this reason, no clear difference was observed between the bubble events for different wall superheats by Siedel *et al.*,[14] except for the growth time. The buoyancy was the main upward force acting on the bubble. The force due the contact area (known as contact pressure force) was the main component of the buoyancy during the first part of the growth, and remained a third of the total buoyancy before detachment. The resultant of the surface tension and adhesion forces acting on the triple line was the only downward force, which balances buoyancy. Its value was very sensitive to the determination of the apparent contact angle.

Thanks to the determination of all individual components of the integral momentum balance, the residuals resulting from the occurring imbalance were used in order to ensure the validity of the force expressions and of the measurement methodology. A non-negligible imbalance directed upwards of the same order of magnitude as the contact pressure force was found. The validity of the apparent contact angle measurements was thus discussed, and the possible mirage effects at the base of the bubble were mentioned.

The bubble contour obtained from the image processing was compared to numerical solutions of the capillary equation fitted to the upper part of the bubble. Evidence of mirage effects at the base of the bubble were highlighted, the refraction of light tending to increase the apparent contact angle towards 90°. The measurements of the apparent contact angle were consequently corrected using the numerical simulation of the bubble profiles.

The computation of the integral momentum balance, including corrected values of the apparent contact angle, showed a much lower imbalance. The imbalance, directed downwards, opens the question of the assumption of a homogeneous surface tension at the saturation temperature in the bubble contour simulation.

The analysis of the integral momentum balance did not provide deep information concerning the bubble detachment. An acceleration of the height of the centre of gravity occurs just before departure, leading to a sudden increase of the liquid inertia. It has, however, not been shown that this perturbation was sufficient to imbalance the force equilibrium. To the authors' opinion, the key to detachment rather lays in the apparent contact angle evolution. Pentane is known to be a highly wetting fluid on most substrates, including polished copper. As the apparent contact angle increases, the advancing contact angle may be reached, causing the liquid to penetrate the nucleation site and provoking the rupture of the base of the bubble. Further study is however needed in order to prove this hypothesis.

This detailed analysis of the forces acting on bubbles when boiling on a artificial nucleation site in a controlled environment provides original data that can be used to benchmark numerical simulation of boiling as well as analytical models predicting boiling and bubble growth.

APPENDIX: MOMENTUM VARIATION DECOMPOSITION

The momentum variation of a deformable particle of variable mass, such as a growing bubble, is expressed in Eq. (2). It can also be expressed as a function of the position vector $\overrightarrow{p}$, which depends on the space and time variables:

$$\overrightarrow{F}_{mom} = \frac{\mathrm{d}}{\mathrm{d}t} \iiint_V \rho_v \overrightarrow{p}(x, y, z, t)\, \mathrm{d}V. \tag{A1}$$

According to Panton (Ref. 28, p. 132), this expression is developed as a function of the position of the center of mass $\overrightarrow{P}_{cg}$ as follows:

$$\overrightarrow{F}_{mom} = \frac{\mathrm{d}}{\mathrm{d}t}\left(\rho_v \frac{\mathrm{d}\overrightarrow{P}_{cg}(x, y, z, t)}{\mathrm{d}t} V(t) - \oint \rho_v \left(\overrightarrow{p}(x, y, z, t) - \overrightarrow{P}_{cg}(x, y, z, t)\right) \overrightarrow{n} \cdot \left(\overrightarrow{v} - \overrightarrow{w}\right) \mathrm{d}S\right) \tag{A2}$$

with $\overrightarrow{v}$ and $\overrightarrow{w}$ being, respectively, the vapour and surface velocity vectors on the interface.

The second term on the right-hand side is due to the difference of velocity between the interface and the vapour at the interface, or, as it is integrated around the interface, to the non-symmetry of the gain of mass. It is sometimes referred to as the *jet effect*.

For a growing bubble, the phase-change distribution around the interface determines the magnitude of the jet effect. Unfortunately, in the case of the present study, the phase-change distribution is unknown *a priori*. It is however possible to estimate the relative magnitude of the jet effect term in the momentum variation for a worst-case scenario. The most non-symmetrical phase-change distribution which is still axisymmetric is to have all the evaporation occurring at the contact line between the interface and the solid surface.

In such a scenario, the vapour and surface velocity are equal everywhere on the interface, except on an infinitesimal area dA close to the triple line. There, the surface velocity is zero and the vapour velocity is normal to the interface so that

$$\overrightarrow{v} = \frac{1}{\mathrm{d}A}\frac{\mathrm{d}V}{\mathrm{d}t}\overrightarrow{n}. \tag{A3}$$

Thus, on the area dA,

$$\overrightarrow{n} \cdot \left(\overrightarrow{v} - \overrightarrow{w}\right) = \frac{1}{\mathrm{d}A}\frac{\mathrm{d}V}{\mathrm{d}t}. \tag{A4}$$

Considering the center of gravity located on the axis of symmetry at a height h_{cg} and the contact line on a circle of radius R_{base}, the axial component of the difference between the position vector and the position of the center of gravity is such that

$$\left(\overrightarrow{p}(x, y, z, t) - \overrightarrow{P}_{cg}(x, y, z, t)\right) = -h_{cg}\overrightarrow{k}. \tag{A5}$$

On the area dA at the vicinity the contact line, the surface unit dS can be expressed as a function of a length unit dl along the contact line:

$$\mathrm{d}S = \frac{\mathrm{d}A}{2\pi R_{base}}\mathrm{d}l. \tag{A6}$$

The momentum can now be decomposed in two terms $\overrightarrow{T}_1$ and $\overrightarrow{T}_2$ as follows:

$$\overrightarrow{F}_{mom} = \frac{\mathrm{d}}{\mathrm{d}t}\left(\overrightarrow{T}_1 + \overrightarrow{T}_2\right), \tag{A7}$$

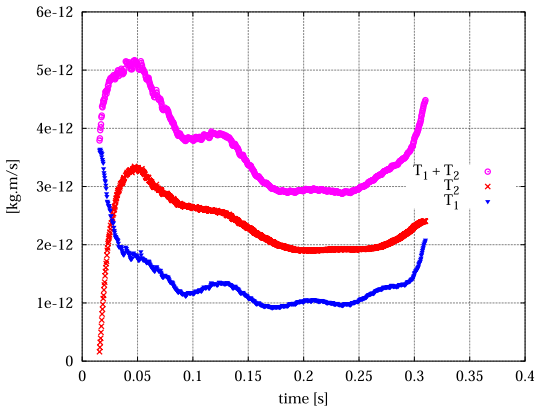

FIG. 16. Comparison of the bubble momentum due to the acceleration of the center of gravity and due to the jet effect.

$$\overrightarrow{T}_1 = \rho_v \frac{\mathrm{d}\overrightarrow{P}_{cg}(x, y, z, t)}{\mathrm{d}t} V(t), \tag{A8}$$

$$\overrightarrow{T}_2 = -\oint \rho_v \left(\overrightarrow{p}(x, y, z, t) - \overrightarrow{P}_{cg}(x, y, z, t)\right) \overrightarrow{n} \cdot \left(\overrightarrow{v} - \overrightarrow{w}\right) \mathrm{d}S. \tag{A9}$$

Due to the axisymmetry assumption, the first term $\overrightarrow{T}_1$ only depends on the height of the center of gravity

$$\overrightarrow{T}_1 = \rho_v \frac{\mathrm{d}h_{cg}}{\mathrm{d}t} \overrightarrow{k}. \tag{A10}$$

The second term $\overrightarrow{T}_2$ can be expressed as a linear integral along the contact line

$$\overrightarrow{T}_2 = \oint \rho_v \frac{h_{cg}}{2\pi R_{base}} \frac{\mathrm{d}V}{\mathrm{d}t} \overrightarrow{k}\, \mathrm{d}l \tag{A11}$$

$$= \rho_v h_{cg} \frac{\mathrm{d}V}{\mathrm{d}t} \overrightarrow{k}. \tag{A12}$$

As both the height of the center of gravity and the volume of the bubble are measured from the images, the two terms of the momentum can be determined and compared, as shown in Figure 16.

It can be seen that both terms are of the same order of magnitude. As the focus is on the time derivative of the momentum, the time evolution of each term is considered. At the beginning of the bubble growth, the first term decreases due to the deceleration of the center of gravity, while the second term increases to to the increase in the height of the center of gravity. The sum of both terms shows a maximum in the overall momentum, but lower absolute values in the slope of the time evolutions. For the second part of the bubble growth, the second momentum term is almost constant and does not affect significantly the momentum variation.

As a conclusion, the assumption of the symmetry of the mass gain during bubble growth (i.e., neglecting the momentum term $\overrightarrow{T}_2$) is valid for the present study as the momentum variation is of the same order of magnitude without this approximation, and as the momentum variation remains negligible compared to the other forces involved.

[1] Lord Rayleigh, "VIII. On the pressure developed in a liquid during the collapse of a spherical cavity," Philos. Mag. Ser. 6 **34**, 94–98 (1917).
[2] M. S. Plesset and A. Prosperetti, "Bubble dynamics and cavitation," Annu. Rev. Fluid Dyn. **9**, 145–185 (1977).
[3] T. H. Cochrane and J. C. Aydelott, "Effects of subcooling and gravity level on boiling in the discrete bubble region," Technical Note TN D-3449 (NASA, 1966).
[4] T. H. Cochrane, J. C. Aydelott, and C. M. Spuckler, "Experimental investigation of nucleate boiling bubble dynamics in normal and zero gravities," Technical Note TN D-4301 (NASA, 1968).

[5] L. Zeng, J. Klausner, and R. Mei, "A unified model for the prediction of bubble detachment diameters in boiling systems," Int. J. Heat Mass Transfer **36**, 2261–2270 (1993).
[6] J. Klausner, R. Mei, D. Bernhard, and L. Zeng, "Vapor bubble departure in forced convection boiling," Int. J. Heat Mass Transfer **36**, 651–662 (1993).
[7] R. Mei and J. Klausner, "Shear lift force on spherical bubbles," Int. J. Heat Fluid Flow **15**, 62–65 (1994).
[8] Y. Buyevich and B. Webbon, "Dynamics of vapour bubbles in nucleate boiling," Int. J. Heat Mass Transfer **39**, 2409–2426 (1996).
[9] G. Duhar, "Croissance et détachement de bulles en paroi d'un écoulement cisaillé: étude expérimentale de l'injection et de l'ébullition nucléée," Ph.D. thesis (Institut National Polythechnique de Toulouse, 2003).
[10] G. Duhar and C. Colin, "Dynamics of bubble growth and detachment in a viscous shear flow," Phys. Fluids **18**, 077101 (2006).
[11] G. Duhar, G. Riboux, and C. Colin, "Vapour bubble growth and detachment at the wall of shear flow," Heat Mass Transfer **45**, 847–855 (2009).
[12] S. Di Bari and A. J. Robinson, "Experimental study of gas injected bubble growth from submerged orifices," Exp. Therm. Fluid Sci. **44**, 124–137 (2013).
[13] F. J. Lesage, J. S. Cotton, and A. J. Robinson, "Analysis of quasi-static vapour bubble shape during growth and departure," Phys. Fluids **25**, 067103 (2013).
[14] S. Siedel, S. Cioulachtjian, and J. Bonjour, "Experimental analysis of bubble growth, departure and interactions during pool boiling on artificial nucleation sites," Exp. Therm. Fluid Sci. **32**, 1504–1511 (2008).
[15] S. Siedel, S. Cioulachtjian, A. Robinson, and J. Bonjour, "Electric field effects during nucleate boiling from an artificial nucleation site," Exp. Therm. Fluid Sci. **35**, 762–771 (2011).
[16] S. Siedel, S. Cioulachtjian, S. Di Bari, A. Robinson, and J. Bonjour, "Analysis of the interface curvature evolution during bubble growth," Heat Transfer Eng. **35**(5), 528–536 (2014).
[17] S. Kandlikar and B. Stumm, "A control volume approach for instigating forces on a departing bubble under subcooled flow boiling," ASME J. Heat Transfer **117**, 990–997 (1995).
[18] Y. Chen, M. Groll, R. Mertz, and R. Kulenovic, "Bubble dynamics of boiling of propane and iso-butane on smooth and enhanced tubes," Exp. Thermal Fluid Sci. **28**(2-3), 171–178 (2004).
[19] N. Ginet, "Analyse des mécanismes contrôlant la croissance et l'ascension d'une bulle isolée en ébullition nucléée," Ph.D. thesis (INSA de Lyon, 1999).
[20] J. Magnaudet, M. Rivero, and J. Fabre, "Accelerated flows past a rigid sphere or a spherical bubble. I. Steady straining flow," J. Fluid Mech. **284**, 97–135 (1995).
[21] D. Legendre, C. Colin, and T. Coquard, "Lift, drag and added mass of a hemispherical bubble sliding and growing on a wall in a viscous linear shear flow," Philos. Trans. R. Soc. London **366**, 2233–2248 (2008).
[22] A. Robinson and R. Judd, "The dynamic of spherical bubble growth," Int. J. Heat Mass Transfer **47**, 5101–5113 (2004).
[23] P.-G. de Gennes, F. Brochard-Wyart, and D. Quéré, Gouttes, bulles, perles et ondes (Belin, 2002).
[24] S. Petrovic, A. Robinson, and R. Judd, "Marangoni heat transfer in subcooled nucleate pool boiling," Int. J. Heat Mass Transfer **47**, 5115–5128 (2004).
[25] R. Marek and J. Straub, "The origin of thermocapillary convection in subcooled nucleate pool boiling," Int. J. Heat Mass Transfer **44**, 619–632 (2001).
[26] M. Cooper, "The "mirage" in boiling," Int. J. Heat Mass Transfer **26**, 1088–1090 (1983).
[27] M. Gentes, G. Rousseaux, P. Couliet, and P.-G. De Gennes, "Resolution of the Young-Laplace equation by a geometrical method using curvature," C. R. Phys. **6**, 1027–1033 (2005).
[28] R. L. Panton, *Incompressible Flow* (John Wiley & Sons, New York, 1984).